# Recycling detoxified cement asbestos slates in the production of ceramic sanitary wares

# RECYCLING DETOXIFIED CEMENT ASBESTOS SLATES IN THE PRODUCTION OF CERAMIC SANITARY WARES

Andrea Bernasconi[a], Luca Pellegrino[b], Fabrizio Vergani[b], Fabrizio Campanale[b], Narcisa Mihaela Marian[c], Lucia Galimberti[b], Matteo Perotti[c], Cecilia Viti[c], Giancarlo Capitani[b*]

[a]*Ideal Standard International, Via Cavassico Inferiore 160, 32026, Borgo Valbelluna (BL), Italy*

[b]*Department of Earth and Environmental Sciences (DISAT), University of Milano-Bicocca, Piazza della Scienza 4, I-20126, Milano, Italy*

[c]*Department of Physical Science, Earth and Environment (DSFTA), University of Siena, V. Laterina 8, I-53100, Siena, Italy*

*corresponding authors: giancarlo.capitani@unimib.it

## ABSTRACT

The recycling of cement asbestos slates (CAS) thermally treated in air at 1100 °C as secondary raw material in the production of Vitreous China (VC) sanitary wares has been investigated. Deactivated cement asbestos powder (DCAP) has been used in individual substitutions (5 wt.%) of quartz and feldspar. The single raw materials, the ceramic technological properties before and after firing, the phases and microstructure evolution during firing, have been investigated with a variety of techniques, including those commonly used for production quality check and instrumental methods for mineralogical analyses. DCAP acts as flux rather than as inert in the firing process,

promoting greification. Although the substituted samples show some critical aspects that need to be addressed before processing, such as the presence of sulphate salts that increase the dispersant demand and the colour of the fired ceramic body, the overall technological properties are comparable to those of normal production, suggesting the possible reuse of DCAP powder in the production of sanitary wares.

**KEYWORDS**:

A Slip casting

A Firing

B Microstructural final

C Mechanical properties

D Mullite

D Silicate

## 1. INTRODUCTION

Asbestos, i.e., the fibrous minerals belonging to the serpentine and amphibole groups [1] employed as raw material worldwide and then banned in almost all countries since 90s because carcinogen, is still abundant in many construction materials and therefore represents a problem for the human health and the environment. Although many

processes aiming either at detoxifying asbestos containing material (ACM) and/or reuse it as secondary raw material have been published (for a summary s. [2,3]), and the European Union encourages such strategies (e.g., [4]), they have never turned into practice at industrial scale, apart from the only example of the Inertam plant at Morcenx, France [5]. The reason is that the solutions currently adopted by law, i.e., i) confinement, ii) encapsulation and iii) landfilling are generally preferred because they are cost-effective [6].

However, none of the aforementioned methods is close to ideal. Confinement, i.e., insulating the ACM from the exterior through a physical barrier, may cause the environment to be exposed again to asbestos fibres in case of careless maintenance operations, extreme natural phenomena, or terrorist attacks. Encapsulation, i.e., the application of special resins to the ACM to block asbestos fibres impeding their release in the environment, is inexorably subject to degradation over time, requiring periodic maintenance. Landfilling does not eliminate the risk that asbestos fibres could be released into the environment, especially in the water table, over time.

It is a fact that the availability of suitable sites for toxic waste confinement becomes increasingly difficult, in developed and highly anthropized countries and in a worldwide society where free soil is disappearing [7], construction and demolition waste increases exponentially [8–10] and natural raw materials are dramatically reducing [11]. For all these reasons, environmentally friendly and recycling solutions need to be developed, so that the ACM-waste management could include: i) an energy sustainable detoxification treatment and ii) a clear recycling route. This would preserve the natural environment from pollution, depleting resources and human health from hazards.

On the other hand, processes aiming to the detoxification of ACM still suffer from critical issues that need to be solved. For instance, the thermal or thermomechanical treatments are effective but very energy consuming, biological methods are poorly effective and chemical methods consume large amounts of reagents and produce highly acidic fluids that require careful disposal [2,3].

Thanks to a recent patent on thermal inertization of cement asbestos slates (CAS), energy sustainability seems feasible [12,13], and as regards recycling, many promising fields have been investigated (e.g., [14–18]and several patents produced [19,20]. However, the strict protocols characterising many established production pathways require a deep control of the starting materials and of their behaviour under processing conditions to confer the suitable technical properties to the final products. Among the investigated fields, the ceramic industry appears as one of the most promising [19,21].

Typical raw materials used to formulate the ceramic body are quartz, feldspars and clays [22,23]. Clays give plasticity and mechanical strength to the slip body. Feldspars act as flux and control the viscous sintering. Quartz is relatively inert and controls the firing shrinkage and gives dimensional stability. The main processing steps are wet grinding of raw material mixtures, slip casting and firing at a maximum temperature in the range of 1100–1250 °C. The final product is composed of a mixture of newly formed mullite and glass, and residual quartz and feldspar [22,24]. However, the partial replacement of conventional raw materials may alter the proportion of these phases in the fired body and even lead to the formation of additional high-temperature phases and modify the microstructure, which in turn may alter

mechanical properties, porosity, chemical resistance, colour, and stain resistance of the product.

In the present paper, we describe the reuse of CAS thermally treated in air at 1100 °C in the production of Vitreous China (VC) sanitary ware, a complex ceramic material where many parameters like rheology of the slurry, chemical/mineralogical composition, particle size distribution and firing conditions strongly affect the technological and aesthetic properties of the final products [22,25–30]. Indeed, sanitary wares must result in very compact products with extremely low porosity, which is essential to impart the material sufficient mechanical properties, low water absorption, resistance to chemicals, abrasion and cleaning agents. These make sanitary wares robust and easy to clean, and thus perfect for installation where hygiene is of primary importance. Finally, even if a glaze is normally applied, the whiteness of the fired body is essential.

The obtained results show that the substitution in the ceramic body of feldspar and quartz with thermally treated and deactivate CAS up to 5 wt.% does not alter substantially the technological and aesthetic properties of the fired body, therefore indicating deactivated CAS as a potentially suitable candidate for the partial substitution of these raw materials.

## 2. EXPERIMENTAL

### 2.1. MATERIALS

The deactivated material used in the experiments comes from the thermal treatment in air at 1100 °C of CAS. Before the experiments, the material was deeply investigated

with a variety of techniques to certify the disappearance of the asbestos fibres and to characterise the resulting powder (for an exhaustive description of the deactivated material see [6,12]. Further tests were performed at the Ideal Standard Laboratory of Trichiana (BL, Italy) with the aim to characterise the deactivated cement asbestos powder (DCAP) from a ceramic-technological point of view. Quartz and feldspar, which represent the potential candidates to be partially substituted in the ceramic slip formulation by the DCAP, have been also characterised. Furthermore, to evaluate the effect of the introduction of the DCAP in a traditional VC sanitary ware, three slurries of ball clays, China clays, Quartz, Na-feldspar and DCAP have been prepared at the laboratory scale (5 Kg of dried material), according with Table 1. Here, sample NP is the normal production composition, representing the benchmark for further evaluation of slip behaviour in the ceramic process. Samples S1 and S2 are designed to evaluate the effect of DCAP introduction in partial substitution (5 wt.%) of filler material like quartz and fluxing agent like Na-feldspar, respectively. The chemical composition of the different raw materials is displayed in Table 2.

## 2.2. SINGLE RAW MATERIALS CERAMIC-TECHNOLOGICAL CHARACTERIZATION

DCAP, quartz and feldspar single raw materials have been characterised by several methods:

- *Particle size distribution (PSD)*. Residue of each raw material at 45 and 75 µm have been determined by sieving in humid conditions. Moreover, laser scattering curves have been measured using a Malvern Mastersizer 3000.

- *pH, Conductivity and Ion Chromatography (IC) test in solution*. These three tests have been performed by means of a Hanna Instruments pH-metre, Hanna Instruments conductivity metre, and Thermo Scientific Dionex Aquion IC system, respectively.

- *Colour after firing*. It has been determined by means of a Konica Minolta CM-700d spectrophotometer using D65 Cielab space. These measurements have been performed after firing in an industrial kiln a pressed sample (around 20 grams) of each single raw material.

- *Upon firing behaviour*. It has been characterised by means of hot stage microscope Camar Microvis. The specimen, a pressed cylinder of about 2 mm diameter and 4 mm height, has been placed on an alumina substrate and fired in the 20-1400°C temperature range, with a ramp-rate of 10°C/min. During the entire ramp, a camera recorded images every minute to monitor the specimen shape evolution (i.e., sintering, softening and melting).

## 2.3 SLIP CERAMIC-TECHNOLOGICAL CHARACTERIZATION

NP, S1 and S2 slip compositions have been characterised by several methods:

- *Density and rheology of the slurry*. Density has been measured by weighing each slurry into a 500-cc capacity pycnometer. Rheology has been measured by means of a Brookfield viscometer using spindle n.3. In particular, the Bingham method [31] has been applied to quantify the plastic viscosity and the yield stress by collecting data at five different shear rates (130, 110, 80, 50 and 30 rpm for 10 s/each).

- *Particle size distribution (PSD)*. For each slurry, the laser scattering curve has been measured using a Malvern Mastersizer 3000.

All the following tests have been performed on samples fired in an industrial tunnel kiln according to the firing cycle reported in Figure 1.

- *Total shrinkage* ($T_s$). For each slip it has been quantified on fired rod by means of equation 1:

$$T_s = (L_0 - L_f)/L_0 * 100 \qquad \text{Eq.1}$$

where $L_0$ is the length of the mould in mm and $L_f$ is the length of the fired rod in mm. These two quantities have been measured by a high precision calliper.

- *Water absorption ($W_A$)*. For each slip it has been determined on the fired rod, following UNI-EN 997 normative. The procedure requires initially weighing the rod ($w_d$) after drying for 12 h at 110°C. Then, the rod is immersed and boiled in water for 2 h, then cooled in situ for 12 h and then re-weighed ($w_w$). The $W_A$ value is calculated by equation 2:

$$W_A = (w_w - w_d)/w_d * 100 \qquad \text{Eq.2}$$

The $W_A$ value represents a technical requirement of the sanitary-ware vitreous body to be accepted in the warehouse, being its limit value equals to 0.5.

- *Mechanical tests*. They have been performed by means of a Monsanto Tensiometer 2000 instrument to measure the Flexural strength (in kg/cm$^2$) and the Young modulus (in GPa). For each slip, 8 different bars have been tested to improve statistics.

- *Linear thermal expansion measurements*. They have been carried out using a Netzsch Dilatomer 402 ED in the 20°C-650°C temperature range, with a heating ramp of

10°C/min. The linear thermal expansion coefficient (α) has been then calculated by Proteus software (from Netzsch) in the desired temperature range following equation 3:

$$\alpha = L_n (1+ d_L/L_0)/(T-T_0) \quad \text{Eq.3}$$

with $d_L$ equals to $L(T)-L(T_0)$, where $L(T)$ and $L(T_0)$ correspond to the measured lengths of the specimen at T and $T_0$, respectively, being the latter set at 30°C. The specimen is a bar of 5 x 5 x 50 mm cut from the total shrinkage fired rod.

- *Colour after firing*. It has been determined by means of a Konica Minolta CM-700d spectrophotometer using D65 Cielab space. These measurements have been performed on the total shrinkage fired rod.

- *Gradient kiln test*. NP and S2 slips have been also characterised using a gradient kiln from Kiln & Furnaces to further investigate their greification behaviour at 6 different peak programmed temperatures (1140, 1160, 1180, 1200, 1220 and 1240 °C, 1 h of soaking time each). Once cooled down, the $W_A$ have been measured for each sample, following the procedure described above in order to draw the greification curve (i.e. Temperature vs. $W_A$ curve).

## 2.4. X-RAY POWDER DIFFRACTION (XRPD)

Fragments of S2 and NP samples fired at temperatures of 1160, 1180, 1200 and 1220 °C were grinded in agate mortar, back loaded into an Al sample holder and analysed by a Bragg–Brentano PANalytical X'Pert-Pro PW3060 diffractometer (θ–θ geometry; CuKα radiation). XRPD data were collected in the 5–80° 2θ range, with step size of 0.02°, at

room temperature, and operating conditions of 40 mA and 40 kV. Qualitative phase analysis was carried out with the PANalytical X'Pert High Score software, using the ICSD PDF2-2004 database. Quantitative phase analysis (QPA) was performed with the Rietveld method [32] using the GSAS II package [33] . To determine the amorphous content, 20 wt.% of α-alumina was added as an internal standard. In order to eliminate any possible amorphous content in the standard that could adversely affect the QPA results [27], corundum was previously annealed at 900 °C for 36 hours in a furnace. The weight fraction of each crystalline phase ($W_\alpha'$) in the studied samples was quantified according to equation 4:

$$W_\alpha' = W_\alpha * (W_c'/W_c) * [1/(1-W_c')] \qquad \text{Eq. 4}$$

where $W_\alpha$ and $W_c$ are the refined weight fractions of phase α and of the internal corundum standard, respectively, and $W_c'$ is the actual added weight of the internal standard (20 wt.%). The actual weight fraction of the amorphous material ($W_g'$) is then calculated as $W_g' = 1 - \Sigma_i W_{\alpha i}'$.

## 2.5. SCANNING ELECTRON MICROSCOPY (SEM)

SEM investigations were performed at the Platform of Microscopy of the University of Milano-Bicocca with a Tescan VEGA TS 5136XM and a Zeiss Gemini 500, both equipped with an energy dispersive system (EDS). Backscatter electron (BSE) images and EDS analyses were acquired on DCAP-bearing samples (S2) and normal production samples (NP) fired at different temperatures (1160, 1180, 1200 and 1220 °C). Fired samples

were prepared as parallelepipeds about 4 x 2 x 0.5 cm with a 4 x 2 cm polished face and carbon coated to avoid electrostatic charging during the observations.

Particle Analysis was carried out to determine the porosity and shape of voids of the NP and S2 samples using the java-based open-source ImageJ/Fiji software. For each sample, four BSE images taken at fixed magnification (200x) and resolution (768x840 pixels), leading to 0.64 pixel/µm, were investigated. A pixel-based segmentation was made using the Fiji plugin 'Trainable weka segmentation', a machine learning tool for pixel classification [34]. This plugin was used to recognize and distinguish the pores and to apply the same conditions to all images. Once the binary images were obtained, the porosity (%) of each image was measured, together with the number of pores and their area and shape (circularity) using the Imagej/Fiji particle analysis tool. For porosity, all pores with an area less than 5 $\mu m^2$ (~2 pixels) were excluded. The final porosity (%) represents the average of the four images in each sample (Table 6). For circularity, all pores with an area less than 22 $\mu m^2$ (~9 pixels) were excluded, to limit the contribution of smaller pores that statistically have circularity of ~1, this because the samples studied in this work show a dimension of the smallest pores which is too close to one pixel at 768x840 resolution.

## 3. RESULTS AND DISCUSSION

### 3.1. CERAMIC TECHNOLOGICAL CHARACTERIZATION

Sanitary ware production follows established protocols which optimise workability of the slurry and technical and aesthetic properties of the final products. Any substitution

of conventional raw materials must not alter these standards. Table 3 summarises the results of single raw materials ceramic technological characterization. The DCAP has a larger average grain size than the substituted raw materials, as demonstrated by the higher residue at 45 and 75 µm and the higher d90 value. Several authors have established a clear relationship between the grain size of filler (inert) material and the final mechanical properties of the fired sanitary body (e.g., [22,28,35]). However, in the present case, as will be shown in the following sections, the DCAP acts as a fluxing agent rather than as inert, and it is completely consumed at the highest firing temperatures. Bernasconi [27] demonstrated that the grain size of feldspar affects the greification process: the finer the grain size, the faster the process. Therefore, it seems that exploiting the interplay between feldspar and DCAP with a suitable selection of their respective grain sizes, the fine tuning of the greification process would be possible.

The conductivity of the DCAP is much higher for the substituted materials, probably related to the higher electrolytes content, i.e., sulphate but also iron and other metals [6]. The colour of DCAP tend to dark and red if compared with the colour of feldspar and quartz, as inferred by the lowest L* and the highest a* values, respectively. The resulting ochreous colour of the DCAP is probably due to oxidation of iron in the starting material during heat treatment in air.

The hot stage microscopy single raw material characterization is reported in Figure 2. The behaviour of the DCAP is in between the fully inert behaviour of quartz and the fluxing role of feldspar. This observation justifies our choice of partially replacing with DCAP these two traditional ceramic raw materials.

Table 4 summarises the results of ceramic slips technological characterization. The high value of sulphates in the DCAP (Table 3) directly affect the slip rheological behaviour, being the presence of soluble salts in solution responsible for flocculation of clay minerals, which increases the slurry viscosity [22,36]. In fact, to reach similar plastic viscosity and yield stress in NP, S1 and S2, the dispersant addition in the case of DCAP-substituted samples is ten times higher than for the NP sample.

The mechanical properties of the DCAP-substituted samples are in line with those of the NP samples in the terms of Young moduli, while the flexural strength is lower than in NP samples (see discussion in the following sections). Both S1 and S2 samples show very low $W_A$ values, suggesting that the DCAP is actively contributing to the greification of the slip upon firing. Moreover, the total shrinkage of both DCAP-substituted samples is in line with the NP sample, suggesting that the partial introduction of the DCAP in the slip formulation would not require modification in the mould modelling.

The fired slip colour is clearly connected with the single raw material after firing colour: both S1 and S2 slips are darker than normal production. This result must be further evaluated when glazing the slip, being the fired glaze colour affected by several parameters like, for example, the colour of the slip below. Both S1 and S2 slips have a lower thermal expansion in the 30-600°C range compared to the normal production. These results need to be carefully considered in parallel with the glaze thermal expansion. This is because the thermal expansion of these two bodies (slip and glaze) need to match, or at least the latter kept lower than the former, being the compressive resistance of glaze higher than its tension resistance.

In light of the promising greification behaviour, the S2 and NP slips were further investigated by gradient kiln in a wider temperature range, to better constrain how the addition of 5 wt% of DCAP may affect the ceramic mixture in comparison to NP. Figure 3 displays the greification curve of the S2 and NP slips in the 1140°C-1240°C temperature range. It must be noted that, although NP has much lower water absorption at 1140 and 1160°C than S2, at the highest investigated temperature the difference between the two slips disappears, suggesting a very similar greification level. That also fulfils the UNI-EN 997 normative, being the water absorption values less than 0.5 by mass at a temperature equals or higher than 1180°C. These results confirm previous results at industrial kiln conditions, indicating that the DCAP acts as a good fluxing agent.

### 3.2. PHASE EVOLUTION WITH TEMPERATURE

It is universally acknowledged that the physical properties of fired ceramic bodies rely on the constituent phases resulting from i) the high temperature reactions involving the starting materials and ii) the developed microstructure (e.g. [22,24,37–40]). In this and the following section these two aspects will be evaluated, in the order.

XRPD results of samples S2 and NP are reported in Table 5. The main difference is represented by feldspar (anorthite 62-66%), present only in the S2 samples, whereas quartz, mullite and abundant amorphous phase are present in both samples at all temperatures. Relative phase abundances and variations with increasing temperature are plotted in Figures 4 and 5.

The S2 samples show a progressive increase with temperature of the amorphous phase (49.1-71.3 wt.%) with a relative decrease of the crystalline phases, in particular feldspar (22.1-11.6 wt.%) and quartz (16.6-8.6 wt.%), as expected. Instead, the newly formed mullite remains in the range 8.5-12.2 wt.%, showing a small increment at 1200 °C and then decreasing again (Table 5), although the differences are probably within the experimental error. No trace of the crystalline phases typical of DCAP (akermanite-gehlenite, bredigite, merwinite and larnite;[6]) were detected in sample S2, probably because they were resorbed during firing or remained in a concentration too low to be detected (< 1 wt.%).

Compared to the S2 samples, NP samples show important differences. At all firing temperatures, NP samples are characterised by lack of feldspar. The remaining phases show a seesaw behaviour, even if quartz generally decreases with increasing temperature (23.2-16 wt.%), and mullite and glass increase. Mullite (12.8-21 wt.%) shows the maximum value at 1200 °C and on average is more abundant than in samples S2. The amorphous phase oscillates around 57.7-66.6 wt.%, showing the lowest value at 1200 °C (Table 5).

The average lower value of mullite in S2 samples in comparison to NP samples offers a possible explanation of the lower value of flexural strength observed in the former. Indeed, according to the “mullite hypothesis” e.g., [22,24], the interlocking network of mullite needles is the major contributor to the mechanical strength. However, other hypotheses and explanations also need to be considered (see ahead).

Overall, the addition of DCAP seems to saturate the melt respect to feldspar, promoting its preservation at expense of quartz and induces lower production of

mullite and higher amount of melt. In other words, it acts as a fluxing agent in place of feldspar and makes quartz less inert. Moreover, it seems to provide a more regular thermal evolution of phase development. These findings open to the possibility for some optimization of the DCAP/feldspar ratio in order to minimise the presence of residual fluxing agent, following two different ways: 1) as a more conservative approach, reducing the amount of DCAP in the slip in order to maintain an upon firing behaviour closer to the NP one; on the other side, the design of a more challenging formulation by further increasing the amount of DCAP in the slip, after previous amelioration of the above mentioned rheological issues.

### 3.3. MICROSTRUCTURE EVOLUTION WITH TEMPERATURE

As outlined above, the developed microstructure plays a prominent role in the determination of the sanitary ware bodies after firing properties. For this reason, the microstructure was investigated by SEM-EDS and particle analysis. Quartz, feldspar and mullite were identified based on the chemical composition, glass since its interstitial nature and silica- and alkali-rich composition, non-reconcilable with any expected crystalline phase. In addition, Ti- and Fe-oxides were detected by SEM-EDS, not detected by XRPD probably because of their low concentration.

All samples are porous, with porosity ranging from ~5 to ~20% (Table 6). In addition, the S2 samples fired at 1160 and 1180 °C show bright regions more than 100 µm in diameter, with ill-defined contours (Figs. 6) and identified as clusters of very fine particles of Ca-Mg-Al silicates. These particles probably derive from the powder of the DCAP admixed to the slip and not reabsorbed during firing at low temperature. They

were not detected either in samples fired at 1200 and 1220 °C, or by XRPD, suggesting that their concentration is very low or that they are completely reabsorbed in the melt at higher temperature.

Quartz grains stand up in BSE images by their intermediate grey colour and subhedral to anhedral habit. Most grains are sub-rounded, with dimensions from few μm to more than 50 μm (Fig. 6). Feldspar, mullite and glass tend to get confused at low magnification because they are intimately intermixed (Figs. 7 and 8). At higher magnification, after fine tuning brightness and contrast, feldspar appears in relatively large (>10 μm) ghost crystals, partially melted, and reabsorbed (Fig. 7). Mullite forms small (few μm), randomly oriented, acicular crystals, brighter than the surrounding glass (Fig. 7). Fe- and Ti-oxides, distinguished by the highest BSE yield, form crystals from ~1 μm to less than 15 μm in size, dispersed in the matrix.

The matrix can therefore be described as a microcrystalline irregular network of BSE-lighter phases in a BSE-darker amorphous groundmass (Fig. 6). Within the groundmass, the micro-scale mullite grains can be distinguished from feldspar and glass thanks to their higher content of Al and much lower Ca, Na and K, as shown in the elemental X-ray map of Figure 8. Overall, for both sample types (NP and S2), the matrix seems to increase with respect to quartz and the remaining porosity (darker features in Fig. 6, s. ahead) with increasing temperature, consistently with XRPD results.

The fact that mullite forms small acicular crystals embedded in the melt, suggests an origin from recrystallization and dissolutions of aluminosilicates in the melt (secondary mullite). Fine, feltlike interlocking mullite needles as those observed in these samples are believed to confer strength (mullite hypothesis) to the porcelain body [22,41–43].

In a few cases, annular fractures around quartz grains were observed (Fig. 8). These fractures are due to different thermal expansion coefficients between the particle and the matrix and have this peculiar form when the particle contracts more than the matrix. Conversely, when the matrix contracts more than the particle, radial fractures are formed within the particle, which is a worse situation since the fractures can easily connect and cause deleterious strength and higher water absorption [22]. However, even if annular fractures represent the “normal” situation, their concentration must be contained since they may also cause deleterious strength. Warshaw and Seider [44] have demonstrated that the quartz grain size controls the development of annular fractures. In particular, fractures form easily around quartz grains with dimensions in the range of 50-150 μm (which is the case of Fig. 8), instead they are much less abundant around quartz grains of 25-50 μm and form only occasionally around quartz grains lower than 10 μm.

### 3.4. PORE PARTICLE ANALYSIS

The pore structure in porcelain sanitary wares is a very important physical property since it determines critical characteristics such as mechanical strength and water absorption. In comparison to NP samples, S2 samples result more porous at all temperatures, although both decrease with increasing firing temperature (Table 6 and Fig. 6). In the S2 samples, the porosity is initially very high (22%) and suddenly decreases with increasing temperature, stabilising at ~9%. In the NP samples, the porosity is low at the lower firing temperatures (6.7%) and oscillates between 4.8 and 7.4% with increasing temperature, confirming the same seesaw behaviour seen with XRDP for phase evolution.

Figure 9 shows the normal and cumulative distribution of the pores' area of all samples at each firing temperature. In all samples, the porosity is dominated by pores with area <40 $\mu m^2$ (about 70-90% of the total pores' area; Tables 1S-3S in the supplementary material). This percentage is always slightly higher in the NP samples, so that in the S2 samples pores' area result larger on average. All samples show a similar trend on both normal and cumulative distribution, except that S2 samples show small percentages of pores with area >500 $\mu m^2$, which reaches ~3% at 1220 °C, absent in the NP sample (Table 1S-3S in the supplementary material). These data on porosity parallel the observations on water absorption only in part. Indeed, porosity decreases with increasing firing temperature, in the S2 samples faster than in the NP samples, but stabilises at higher porosity values in S2 samples, contrary to water absorption, which results lower in S2 samples. This further suggests that the observed porosity is not interconnected, therefore limiting water absorption. The higher porosity of S2 samples, however, could be responsible for the lower flexural strength observed. Indeed, it is believed that the predominant factor affecting the strength of porcelain bodies is the density of flaws, here represented by pores [22].

To better understand porosity data, the variation of the cumulative distribution of circularity with increasing temperature has been reported in Figure 10. As a general trend, for both samples, circularity increases with increasing temperature, with few exceptions. For instance, the curves of samples NP_1180 and NP_1200 and of samples S2_1200 and S2_1220 exchange their relative position. Moreover, for sample S2, less regular and comparable trends are observed, with the S2_1160 curve showing a markedly lower average circularity. In spite of these minor oddities, which may be intrinsic of the measuring method (i.e., limited number of investigated samples, image

quality, etc.), and in part reflects the seesaw trends observed for other measured properties (i.e., phase abundances), the observed circularity increase with temperature indicates that the pore structure changes from irregular, interconnected pores at low temperature to isolated, sealed, round pores at high temperature, and explains the lower water absorption of the investigated materials. That is a very important property of sanitary ware ceramic bodies, which results in more stain-resistant and are easier to clean.

## 4. CONCLUDING REMARKS

The reuse of DCAP in sanitary ware vitreous china in substitution of 5 wt.% of quartz or feldspar presents some advantages and disadvantages as compared to normal production. The DCAP secondary raw material presents an ochreous colour due to oxidation of Fe-bearing phases during the deactivation process, which determines a darker fired slip colour of DCAP-substituted samples. Since the colour of the slip affects the fired glaze colour, the final aesthetic properties in case of sanitary whitewares must be preventively assessed. No major problems are envisaged in case of coloured sanitary wares.

Although the reasons that determine the colloidal stability of clays is a complex matter, we retain the large amount of sulphates in the DCAP responsible for clay minerals flocculation, which in turn determines a critical increase of slurry viscosity. This effect is clearly undesired in the ceramic process because it hinders slip preparation procedure as well as casting into plaster and/or resin moulds. To avoid this, a large amount of dispersant must be added, which affects the production costs.

Since sulphates are highly soluble in water, a washing pre-treatment of the DACP before usage should quickly leachate soluble salts avoiding abnormal addition of dispersant, saving money and lengthening only marginally the process time.

It has been observed that DCAP acts as a fluxing agent more than as inert. Its addition limits feldspar consumption and mullite formation. This in turn affects mechanical properties of the slip, with a decrease of flexural strength, but still within acceptable limits. Overall, important technological properties such as water absorption are as good as (or even better than) in normal production. This is due to a high level of greification of the DCAP-substituted samples and consequent low and sealed porosity.

In conclusion, the recycling of DCAP as secondary raw material in sanitary ware production, as for other similar ceramics (stoneware), appears feasible, providing some critical aspects such as soluble salts content and colour of the DCAP, could be properly managed.

## 5. ACKNOWLEDGEMENTS

This paper is an outcome of the projects DEAR, “Deativazione Efficiente dell’Amianto e Riutilizzo, funded by the Italian Ministry of the Ecologic Transition and A-FIRE, “Asbestos Fast Inertization and Recycling”, funded by Fondazione Cariplo within the call “Cariplo 2020 – Circular Economy for a Sustainable Future”.

## 6. REFERENCES

[1] A.F. Gualtieri, Mineral fibres: crystal chemistry, chemical-physical properties, biological interaction and toxicity, (2017).

[2] D. Spasiano, F. Pirozzi, Treatments of asbestos containing wastes, Journal of Environmental Management. 204 (2017) 82–91. https://doi.org/10.1016/j.jenvman.2017.08.038.

[3] V. Paolini, L. Tomassetti, M. Segreto, D. Borin, F. Liotta, M. Torre, F. Petracchini, Asbestos treatment technologies, Journal of Material Cycles and Waste Management. 21 (2019) 205–226. https://doi.org/10.1007/s10163-018-0793-7.

[4] European Parliament resolution of 14 March 2013 on asbestos related occupational health threats and prospects for abolishing all existing asbestos (2012/2065(INI)), 2013. http://www.who.int/ipcs/features/10chemicals_en.pdf.

[5] INERTAM, (n.d.). https://www.inertam.com/ (accessed June 9, 2022).

[6] F. Vergani, L. Galimberti, N.M. Marian, G. Giorgetti, C. Viti, G.C. Capitani, Thermal decomposition of cement–asbestos at 1100 °C: how much “safe” is “safe”?, Journal of Material Cycles and Waste Management. 24 (2022) 297–310. https://doi.org/10.1007/s10163-021-01320-6.

[7] A. Strollo, D. Smiraglia, R. Bruno, F. Assennato, L. Congedo, P. de Fioravante, C. Giuliani, I. Marinosci, N. Riitano, M. Munafò, Land consumption in Italy, Journal of Maps. 16 (2020) 113–123. https://doi.org/10.1080/17445647.2020.1758808.

[8] A. Laurent, I. Bakas, J. Clavreul, A. Bernstad, M. Niero, E. Gentil, M.Z. Hauschild, T.H. Christensen, Review of LCA studies of solid waste management systems – Part I: Lessons learned and perspectives, Waste Management. 34 (2014) 573–588. https://doi.org/https://doi.org/10.1016/j.wasman.2013.10.045.

[9] Z. Tang, W. Li, V.W.Y. Tam, C. Xue, Advanced progress in recycling municipal and construction solid wastes for manufacturing sustainable construction materials, Resources, Conservation & Recycling: X. 6 (2020) 100036. https://doi.org/10.1016/J.RCRX.2020.100036.

[10] X. Zhang, J. Chen, J. Jiang, J. Li, R.D. Tyagi, R.Y. Surampalli, The potential utilization of slag generated from iron- and steelmaking industries: a review, Environmental Geochemistry and Health. 42 (2020) 1321–1334. https://doi.org/10.1007/s10653-019-00419-y.

[11] E. Commission, I. Directorate-General for Internal Market Entrepreneurship and SMEs, S. Bobba, P. Claudiu, D. Huygens, P. Alves Dias, B. Gawlik, E. Tzimas, D. Wittmer, P. Nuss, M. Grohol, H. Saveyn, F. Buraoui, G. Orveillon, T. Hámor, S. Slavko, F. Mathieux, M. Gislev, C. Torres De Matos, G. Blengini, F. Ardente, D. Blagoeva, E. Garbarino, Report on critical raw materials and the circular economy, Publications Office, 2018. https://doi.org/doi/10.2873/167813.

[12] N.M. Marian, G. Giorgetti, C. Magrini, G.C. Capitani, L. Galimberti, A. Cavallo, R. Salvini, C. Vanneschi, C. Viti, From hazardous asbestos containing wastes (ACW) to new secondary raw material through a new sustainable inertization process: A multimethodological mineralogical study, Journal of Hazardous Materials. 413 (2021) 125419. https://doi.org/10.1016/j.jhazmat.2021.125419.

[13] G.S.T.P. Chiurli Gabriele, Impianto mobile/componibile per l'inertizzazione di materiali contenenti amianto, Patent n. 102017000025588, 2019.

[14] A.F. Gualtieri, M. Boccaletti, Recycling of the product of thermal inertization of cement–asbestos for the production of concrete, Construction and Building

Materials. 25 (2011) 3561–3569. https://doi.org/10.1016/J.CONBUILDMAT.2011.03.049.

[15] A.F. Gualtieri, C. Giacobbe, L. Sardisco, M. Saraceno, M. Lassinantti Gualtieri, G. Lusvardi, C. Cavenati, I. Zanatto, Recycling of the product of thermal inertization of cement-asbestos for various industrial applications, Waste Management. 31 (2011) 91–100. https://doi.org/10.1016/j.wasman.2010.07.006.

[16] R. Kusiorowski, T. Zaremba, J. Piotrowski, J. Podwórny, Utilisation of cement-asbestos wastes by thermal treatment and the potential possibility use of obtained product for the clinker bricks manufacture, Journal of Materials Science. 50 (2015) 6757–6767. https://doi.org/10.1007/s10853-015-9231-6.

[17] M.L. Ligabue, A.F. Gualtieri, M. Lassinantti Gualtieri, D. Malferrari, G. Lusvardi, Recycling of thermally treated cement-asbestos for the production of porcelain stoneware slabs, Journal of Cleaner Production. 247 (2020) 119084. https://doi.org/10.1016/J.JCLEPRO.2019.119084.

[18] M. Pérez -Estébanez, P. Mácova, P. Šašek, A. Viani, A. Gualtieri, Mg-Phosphate Ceramics Produced from the Product of Thermal Transformation of Cement-Asbestos, Journal of the Polish Mineral Engineering Society. (2014).

[19] G. Belardi, D. Maccari, A.M. Marabini, P. Plescia, Process for producing ceramic type materials by processing waste containing asbestos and clay, Patent No WO199822410A1. (1998).

[20] T.O.G.S.T.P. Chiurli Gabriele, Procedimento per la preparazione di materiale ceramico e refrattario utilizzando forsterite e larnite, sottoprodotti ottenuti da

un impianto d'inertizzazione di materiali in cemento-amianto, Patent n. 102017000128889., 2020.

[21] A.F. Gualtieri, A. Tartaglia, Thermal decomposition of asbestos and recycling in traditional ceramics, Journal of the European Ceramic Society . 20 (2000) 1409–1418.

[22] W.M. Carty, U. Senapati, Porcelain—raw materials, processing, phase evolution, and mechanical behavior, Journal of the American Ceramic Society. 81 (1998) 3–20.

[23] W.E. Worrall, Ceramic Raw Materials: Institute of Ceramics Textbook Series, Elsevier, 2013.

[24] M. Lassinantti Gualtieri, M. Romagnoli, A.F. Gualtieri, Influence of body composition on the technological properties and mineralogy of stoneware: A DOE and mineralogical–microstructural study, J Eur Ceram Soc. 31 (2011) 673–685. https://doi.org/10.1016/J.JEURCERAMSOC.2010.12.002.

[25] T. Tarvornpanich, G.P. Souza, W.E. Lee, Microstructural evolution in clay-based ceramics I: Single components and binary mixtures of clay, flux, and quartz filler, Journal of the American Ceramic Society. 91 (2008) 2264–2271. https://doi.org/10.1111/j.1551-2916.2008.02393.x.

[26] T. Tarvornpanich, G.P. Souza, W.E. Lee, Microstructural evolution in clay-based ceramics II: Ternary and quaternary mixtures of clay, flux, and quartz filler, Journal of the American Ceramic Society. 91 (2008) 2272–2280. https://doi.org/10.1111/j.1551-2916.2008.02394.x.

[27] A. Bernasconi, N. Marinoni, A. Pavese, F. Francescon, K. Young, Feldspar and firing cycle effects on the evolution of sanitary-ware vitreous body, Ceramics International. 40 (2014) 6389–6398. https://doi.org/10.1016/j.ceramint.2013.11.139.

[28] A. Bernasconi, V. Diella, A. Pagani, A. Pavese, F. Francescon, K. Young, J. Stuart, L. Tunnicliffe, The role of firing temperature, firing time and quartz grain size on phase-formation, thermal dilatation and water absorption in sanitary-ware vitreous bodies, J Eur Ceram Soc. 31 (2011) 1353–1360. https://doi.org/10.1016/J.JEURCERAMSOC.2011.02.006.

[29] A. Bernasconi, V. Diella, N. Marinoni, A. Pavese, F. Francescon, Influence of composition on some industrially relevant properties of traditional sanitary-ware glaze, Ceramics International. 38 (2012) 5859–5870. https://doi.org/10.1016/J.CERAMINT.2012.04.037.

[30] J. Martín-Márquez, J.M. Rincón, M. Romero, Effect of firing temperature on sintering of porcelain stoneware tiles, Ceramics International. 34 (2008) 1867–1873. https://doi.org/10.1016/J.CERAMINT.2007.06.006.

[31] G. Zhang, Y. Wang, J. Ma, Bingham plastic fluid flow model for ceramic tape casting, Materials Science and Engineering: A. 337 (2002) 274–280. https://doi.org/10.1016/S0921-5093(02)00043-6.

[32] H.M. Rietveld, A profile refinement method for nuclear and magnetic structures, Journal of Applied Crystallography. 2 (1969) 65–71. https://doi.org/10.1107/S0021889869006558.

[33] B.H. Toby, R.B. von Dreele, GSAS-II: the genesis of a modern open-source all purpose crystallography software package, Journal of Applied Crystallography. 46 (2013) 544–549. https://doi.org/10.1107/S0021889813003531.

[34] I. Arganda-Carreras, V. Kaynig, C. Rueden, K.W. Eliceiri, J. Schindelin, A. Cardona, H. Sebastian Seung, Trainable Weka Segmentation: a machine learning tool for microscopy pixel classification, Bioinformatics. 33 (2017) 2424–2426. https://doi.org/10.1093/bioinformatics/btx180.

[35] G.P. Souza, P.F. Messer, W.E. Lee, Effect of varying quartz particle size and firing atmosphere on densification of Brazilian clay-based stoneware, in: Journal of the American Ceramic Society, 2006: pp. 1993–2002. https://doi.org/10.1111/j.1551-2916.2006.00986.x.

[36] J., & G.C.M. Heinrich, Introduction to Ceramics Processing, 2014.

[37] B.L.F.A.L.C.M.T.S.D. Barbieri L, Relationship between microstructure and mechanical properties in fully vitrified stoneware, Ceramics: charting the future, Modena, 1995.

[38] C. Leonelli, F. Bondioli, P. Veronesi, M. Romagnoli, T. Manfredini, G.C. Pellacani, V. Cannillo, Enhancing the mechanical properties of porcelain stoneware tiles: a microstructural approach, J Eur Ceram Soc. 21 (2001) 785–793.

[39] P.M.T. Cavalcante, M. Dondi, G. Ercolani, G. Guarini, C. Melandri, M. Raimondo, E.R. e Almendra, The influence of microstructure on the performance of white porcelain stoneware, Ceramics International. 30 (2004) 953–963.

[40] A. Pagani, F. Francescon, A. Pavese, V. Diella, Sanitary-ware vitreous body characterization method by optical microscopy, elemental maps, image processing and X-ray powder diffraction, J Eur Ceram Soc. 30 (2010) 1267–1275. https://doi.org/10.1016/j.jeurceramsoc.2009.11.008.

[41] T.F. Choo, M.A.M. Salleh, K.Y. Kok, K.A. Matori, A review on synthesis of mullite ceramics from industrial wastes, Recycling. 4 (2019). https://doi.org/10.3390/recycling4030039.

[42] L. Carbajal, F. Rubio-Marcos, M.A. Bengochea, J.F. Fernandez, Properties related phase evolution in porcelain ceramics, J Eur Ceram Soc. 27 (2007) 4065–4069. https://doi.org/10.1016/J.JEURCERAMSOC.2007.02.096.

[43] N. Marinoni, A. Pagani, I. Adamo, V. Diella, A. Pavese, F. Francescon, Kinetic study of mullite growth in sanitary-ware production by in situ HT-XRPD. The influence of the filler/flux ratio, J Eur Ceram Soc. 31 (2011) 273–280. https://doi.org/10.1016/j.jeurceramsoc.2010.10.002.

[44] S.I. Warshaw, R. Seider, Comparison of strength of triaxial porcelains containing alumina and silica, Journal of the American Ceramic Society. 50 (1967) 337–343.

**Captions to figures and tables**

**Figure 1**: Industrial firing cycle used for after firing behaviour characterization.

**Figure 2**. hot stage microscopy curves of DCAP (red line), quartz (blue line) and feldspar (green line).

**Figure 3**. Greification curves of NP slip (green squares) and S2 slip (red circles).

**Figure 4**. Plot of the relative phase abundances determined in sample S2 at different firing temperatures

**Figure 5**. Plot of the relative phase abundances determined in sample NP at different firing temperatures.

**Figure 6**. BSE images of NP (left column) and S2 (right column) samples fired at 1160 °C, 1180 °C, 1200 °C, 1220 °C. Qtz = quartz. Arrows indicate Ca-Mg-Al silicates clusters of admixed deactivated CA slates powder. For explanation see text. Scale bar: 50 µm.

**Figure 7**. BSE image of sample S2_1200. Quartz grains (Qtz) appear fragmented and rounded; feldspar (Fsp) partially melted and strongly resorbed. We also observe a widespread irregular network with a brighter BSE signal embedded in a BSE-darker groundmass. Part of the BSE-brighter part consists of a microcrystalline acicular mullite (arrows); the darker one of glass.

**Figure 8**. BSE image (A) and related X-ray map (B) of a portion of sample S2_1200. The major element map (Si, Al, Ca, Na, K) shows that the microcrystalline grains in the matrix are separated into two geochemically distinct domains, i.e. an Al-rich (alkali absent)

domains in red and an alkali-rich (Al-poor) domains in blue. Quartz grains are highlighted in green (Si-rich). Note the annular fracture around the large quartz grain on the left.

**Figure 9**. Comparison of the normal and cumulative distribution of the pores' area for S2 and NP samples at 1160, 1180, 1200, and 1220 °C.

**Figure 10**. NP vs S2 cumulative distribution of circularity with increasing temperature.

**Table 1**. Raw materials composition of the prepared slurries.

**Table 2**: Elemental composition of the raw materials used for the initial slip composition. Average uncertainty about 1%.

**Table 3**. Results summary of the raw material ceramic technological characterization.

**Table 4**. Results summary of the ceramic slips technological characterization.

**Table 5**. Quantitative phase analysis for sample S2 and NP detected at different firing temperatures.

**Table 6**. Porosity (%) affecting the studied samples as measured through particle analysis image processing.

**Declaration of interests**

☒ The authors declare that they have no known competing financial interests or personal relationships that could have appeared to influence the work reported in this paper.

☐The authors declare the following financial interests/personal relationships which may be considered as potential competing interests:

| |
|---|
| |

Table 1. Raw materials composition of the prepared slurries.

| Sample ID | Ball clay (wt.%) | China clay (wt.%) | Quartz (wt.%) | Na-Feldspar (wt.%) | DCAP (wt.%) |
|---|---|---|---|---|---|
| NP | 26.5 | 25 | 19 | 29.5 | 0 |
| S1 | 26.5 | 25 | 14 | 29.5 | 5 |
| S2 | 26.5 | 25 | 19 | 24.5 | 5 |

NP = normal production; S1 = quartz DCAP-substituted formulation; S2 = feldspar DCAP-substituted formulation.

Table 2: Elemental composition of the raw materials used for the initial slip composition. Average uncertainty about 1%

| Raw materials (wt.%) | $SiO_2$ | $Al_2O_3$ | $Fe_2O_3$ | MnO | MgO | $TiO_2$ | CaO | $K_2O$ | $Na_2O$ | $SO_3$ | LOI (%) |
|---|---|---|---|---|---|---|---|---|---|---|---|
| Ball clay* | 50.8 | 32.6 | 1.21 | - | 0.25 | 0.95 | 0.2 | 1.72 | 0.21 | - | 12.07 |
| China clay* | 48.23 | 36.68 | 0.95 | - | 0.05 | 0.15 | 0.19 | 1.77 | 0.08 | - | 11.9 |
| Quartz* | 99.37 | 0.4 | 0.04 | - | 0.01 | 0.01 | 0.02 | 0.05 | 0.05 | - | 0.05 |
| Na-Feldspar* | 69.9 | 18.1 | 0.12 | - | 0.2 | 0.25 | 0.5 | 0.3 | 10.3 | - | 0.33 |
| DCAP** | 30.41 | 3.9 | 5.94 | 0.43 | 7.68 | 0.23 | 47.38 | 0.42 | 0.17 | 3.11 | 0.32 |

* From the datasheet of the provider. ** EDXRF data (major components) from [6].

Table 3. Results summary of the raw material ceramic technological characterization.

| | DCAP | Feldspar | Quartz |
|---|---|---|---|
| Residue at 45 µm (wt.%) | 33 | 8 | 10.7 |
| Residue at 75 µm (wt. %) | 19.7 | 1.1 | 1.8 |
| d10 (µm) | 1.55 | 1.6 | 2.1 |
| d50 (µm) | 12.4 | 11.4 | 16.5 |
| d90 (µm) | 142 | 42.4 | 52.3 |
| pH | 10 | 8 | 9.8 |
| Conductivity (µS) | 10000 | 82 | 40 |
| Sulphate (ppm) | 10238 | 221.9 | 124.3 |
| Chloride (ppm) | 62.9 | 42.6 | 36 |
| L* | 62.86 | 73.95 | 94.68 |
| a* | 9.71 | 1.58 | 1.35 |
| b* | 23.44 | 19.65 | 3.97 |

Table 4. Results summary of the ceramic slips technological characterization.

| | NP | S1 | S2 |
|---|---|---|---|
| Density (g/l) | 1850 | 1848 | 1849 |
| Plastic viscosity (cP) | 541 | 476 | 484 |
| Yield stress (dyn/cm$^2$) | 73 | 85 | 108 |
| d10 (µm) | 1.6 | 1.6 | 1.6 |
| d50 (µm) | 10.4 | 10 | 10.3 |
| d90 (µm) | 47.8 | 46.6 | 47.1 |
| Total shrinkage (%) | 10.6 | 10.3 | 10.6 |
| WA (%) | 0.15 | 0.02 | 0.01 |
| Flexural strength (kg/cm$^2$) | 630 | 586 | 537 |
| Young modulus (GPa) | 21 | 23 | 23 |
| α from 30 to 600°C (1/°C) | 7.21 | 6.65 | 6.76 |
| L* | 80.87 | 70.01 | 70.58 |
| a* | 0.9 | 1.1 | 1.1 |
| b* | 9.6 | 9.04 | 8.62 |

Table 5. Quantitative phase analysis for sample S2 and NP detected at different firing temperatures

| | S2_1160 | S2_1180 | S2_1200 | S2_1220 |
|---|---|---|---|---|
| Qtz | 16.6 | 13.7 | 12.6 | 8.6 |
| Mul | 12.2 | 9.1 | 10.8 | 8.5 |
| Fsp | 22.1 | 17.3 | 15.4 | 11.6 |
| Glass | 49.1 | 59.9 | 61.2 | 71.3 |
| | NP_1160 | NP_1180 | NP_1200 | NP_1220 |
| Qtz | 23.2 | 20.6 | 21.3 | 16 |
| Mul | 13.4 | 12.8 | 21 | 17.5 |
| Fsp | 0 | 0 | 0 | 0 |
| Glass | 63.4 | 66.6 | 57.7 | 66.6 |

Table 6. Porosity (%) affecting the studied samples as measured through particle analysis image processing

| | 1160 | 1180 | 1200 | 1220 |
|---|---|---|---|---|
| S2 | 22% | 9.50% | 9.60% | 9.20% |
| NP | 6.70% | 7.40% | 4.80% | 5.40% |

Figure 1

Click here to access/download;Figure;Fig1.tiff

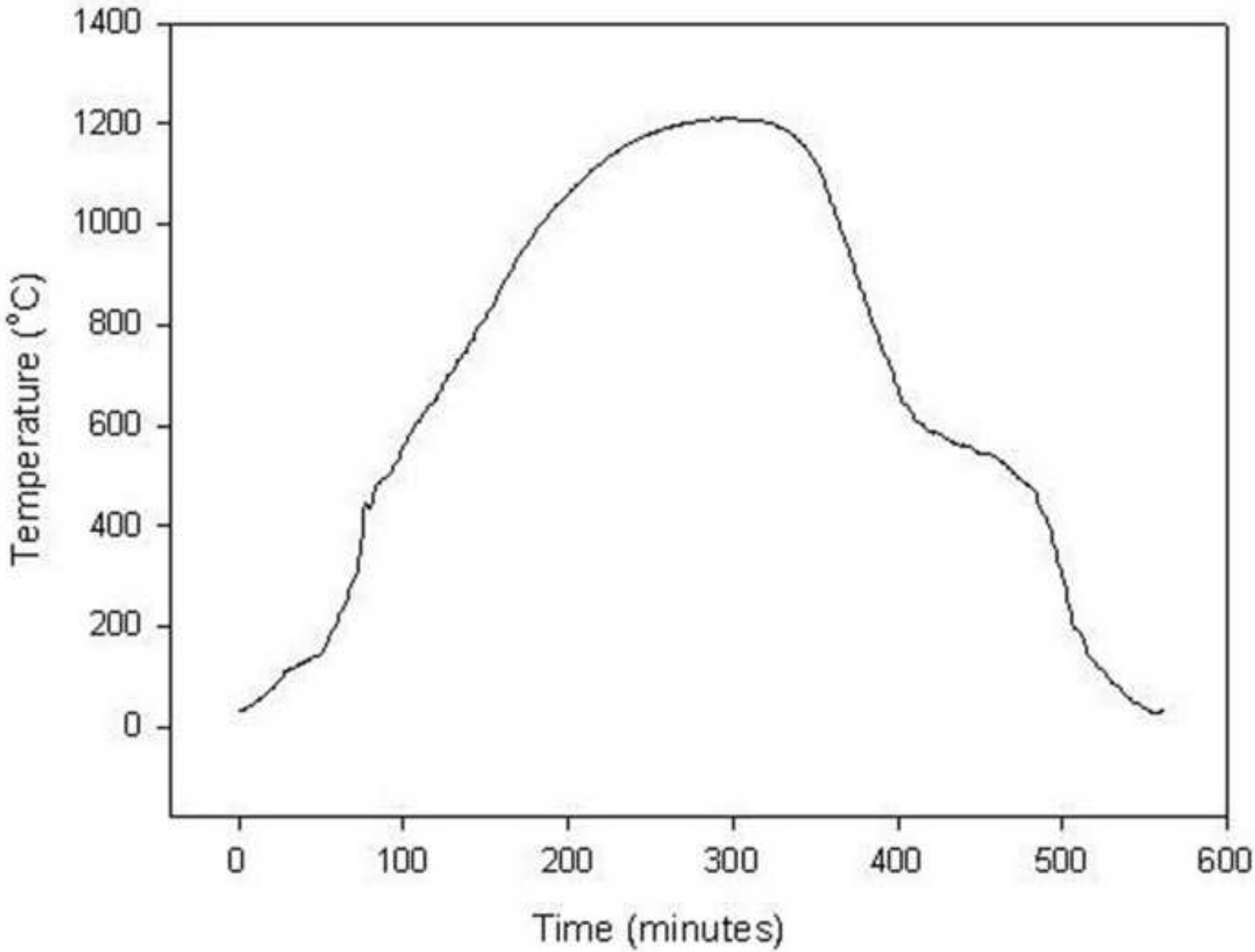

Figure 2



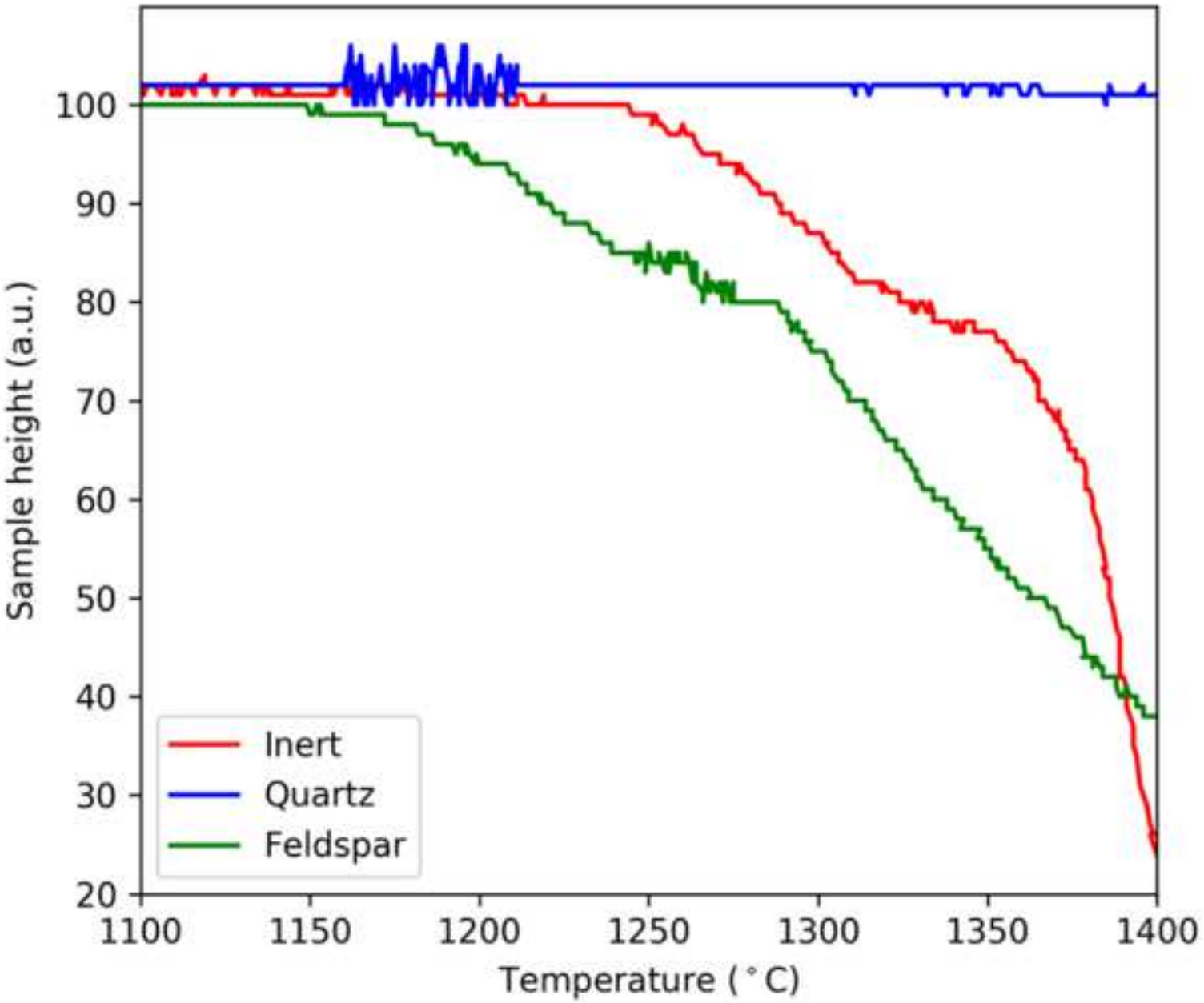

Figure 3

Click here to access/download;Figure;Fig3.tiff

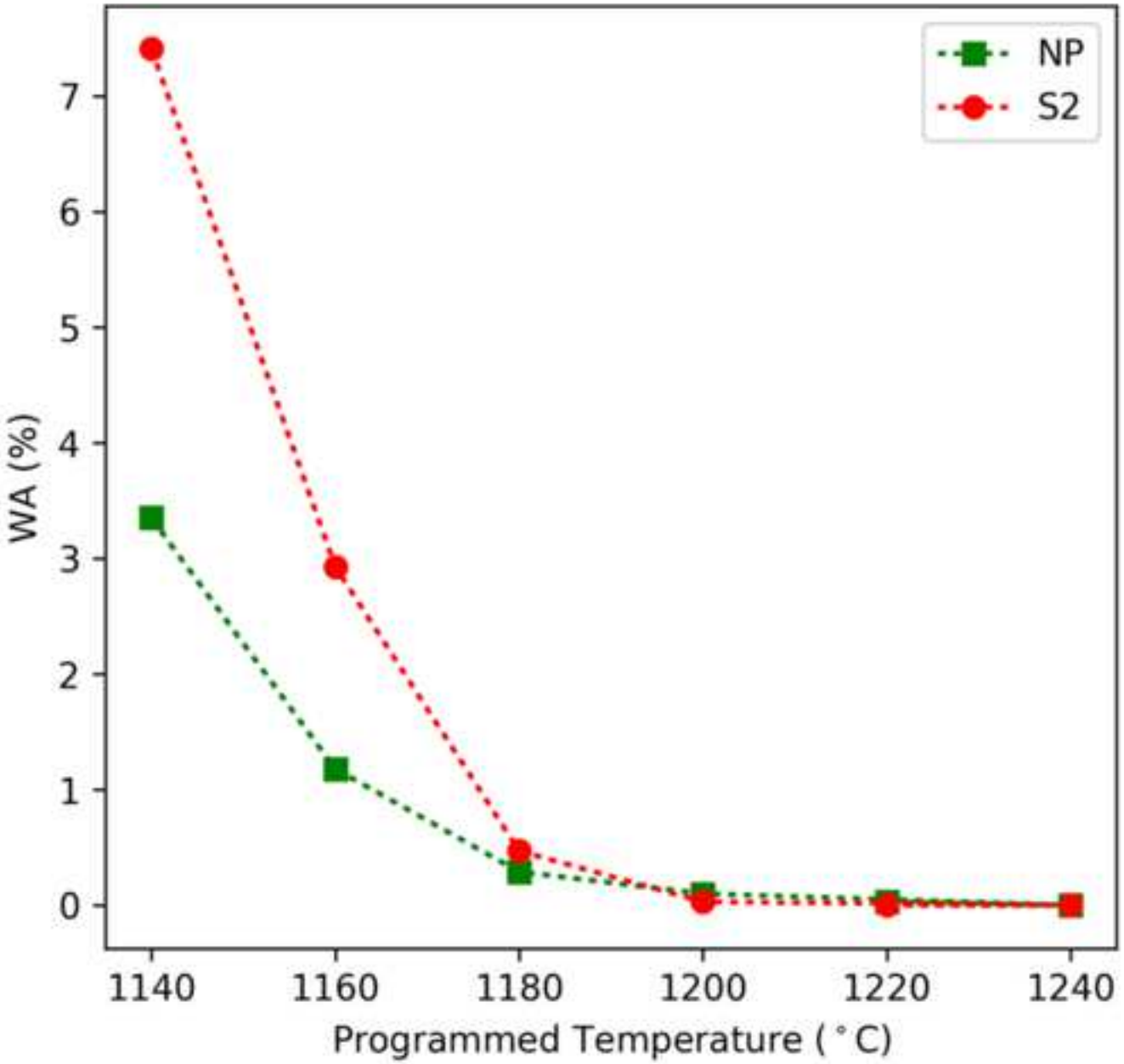

Figure 4

Click here to access/download;Figure;Fig.4.tif

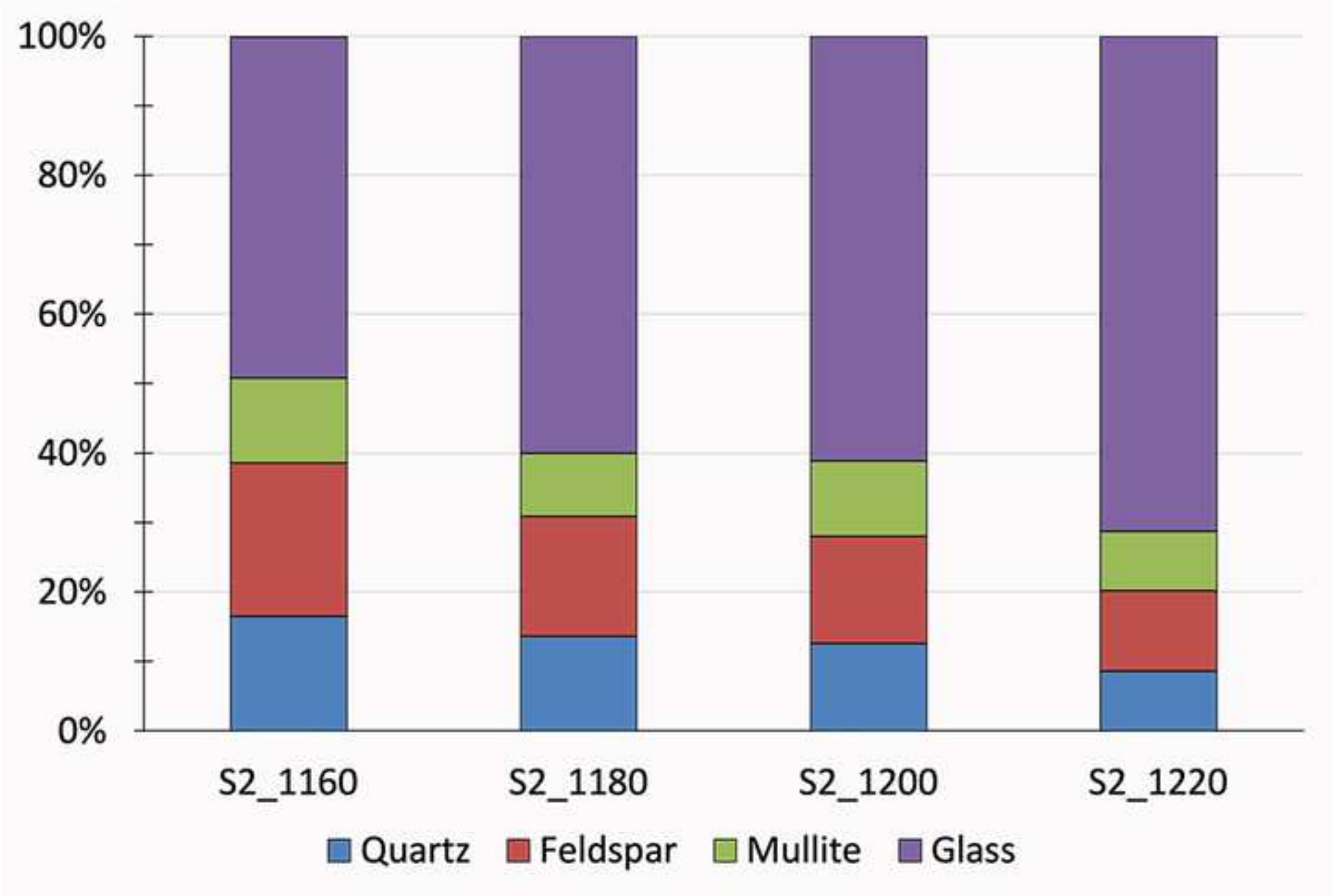

Figure 5

Click here to access/download;Figure;Fig.5.tif

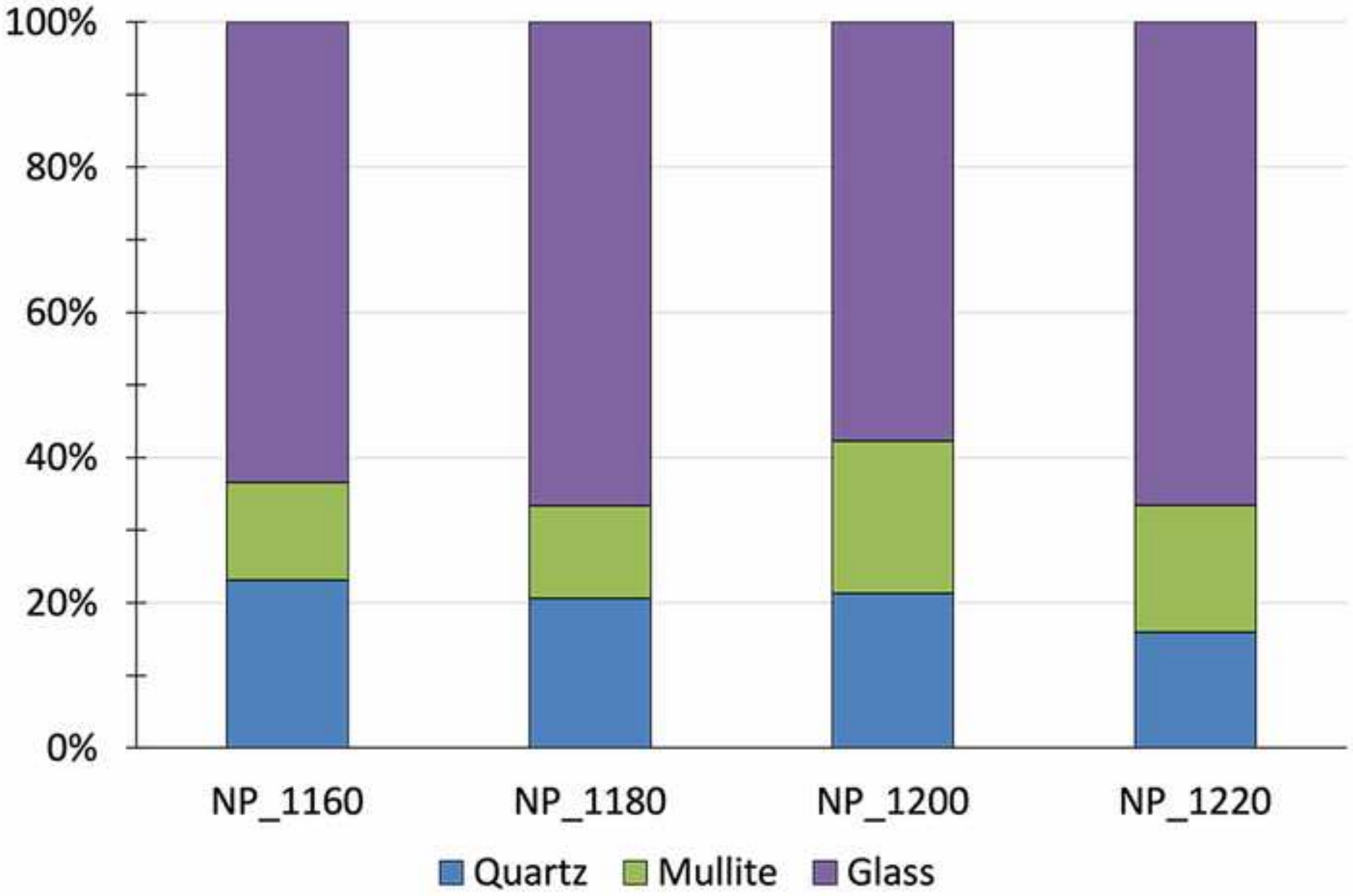

Figure 6

Click here to access/download;Figure;Fig.6.tif

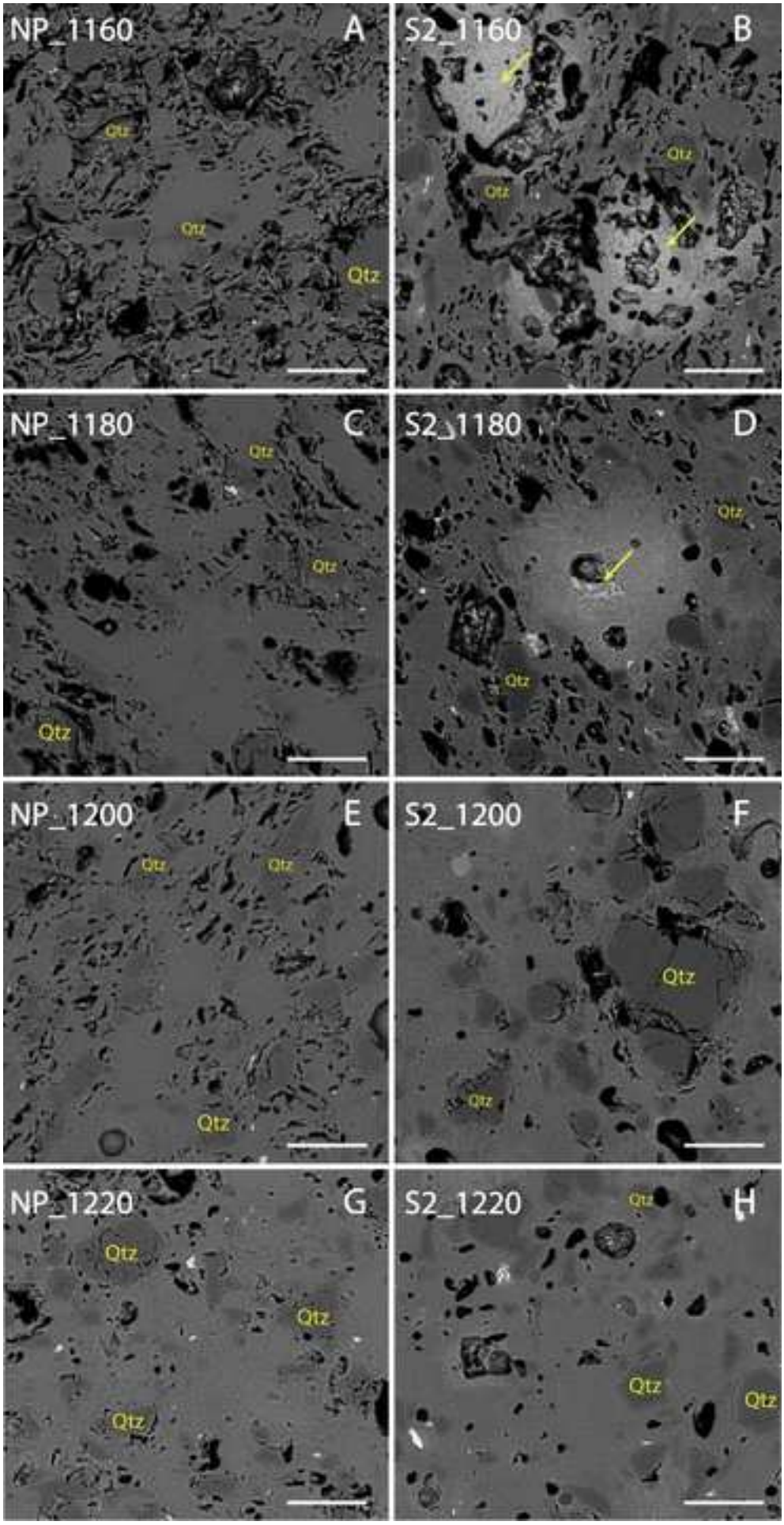

Figure 7

Click here to access/download;Figure;Fig.7.tif

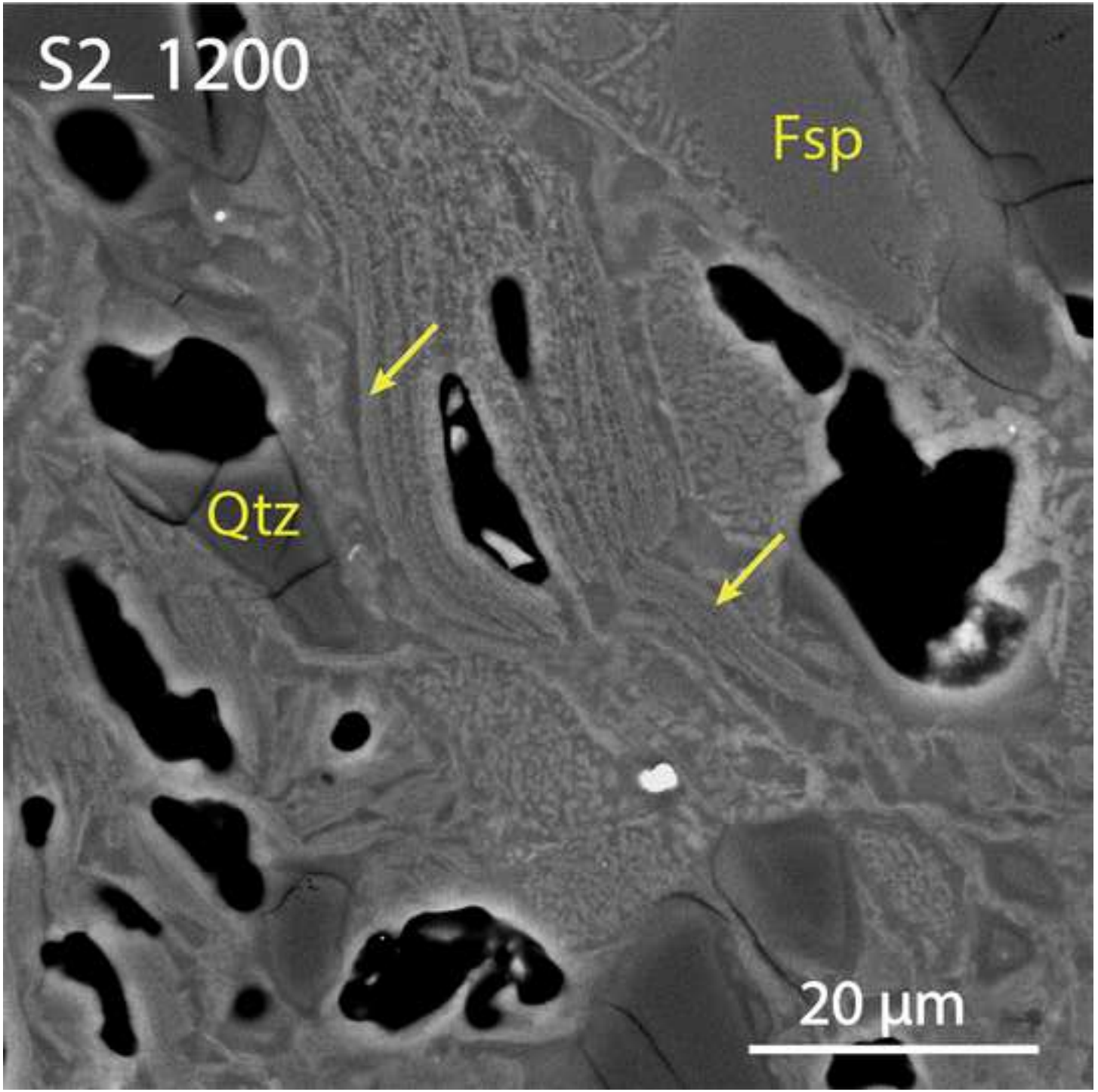

Figure 8



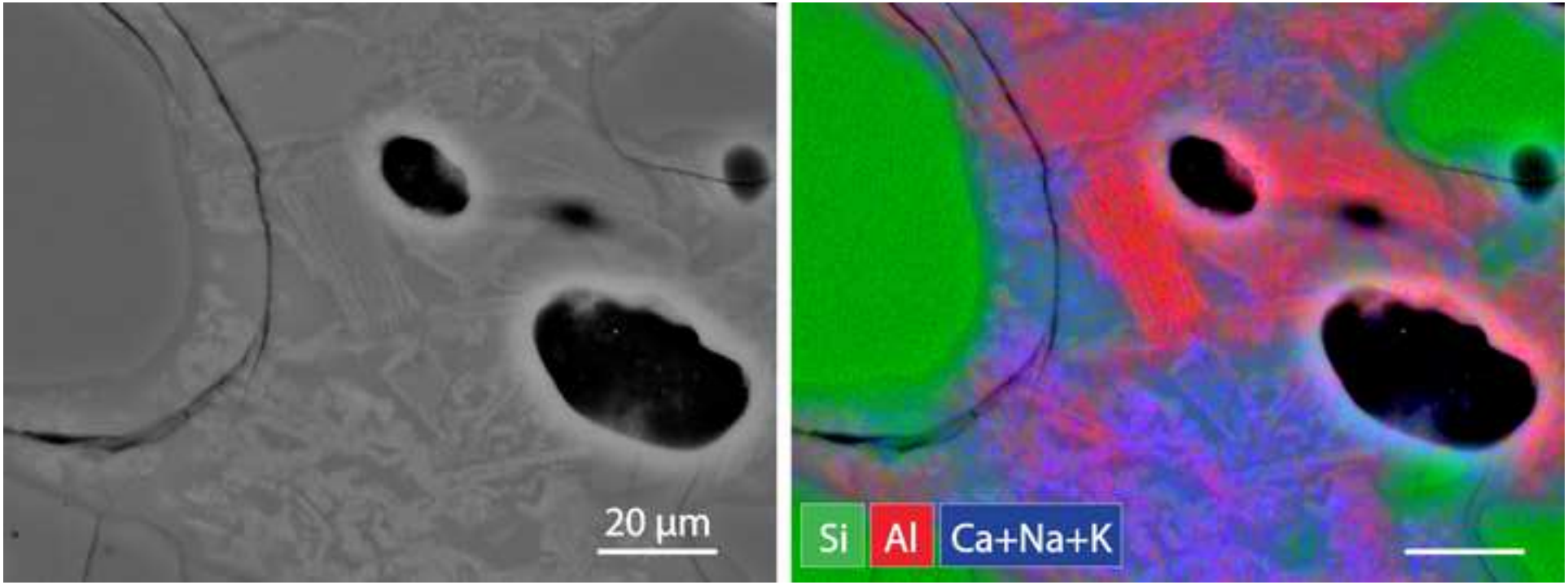

Figure 9

Click here to access/download;Figure;Fig.9.tif

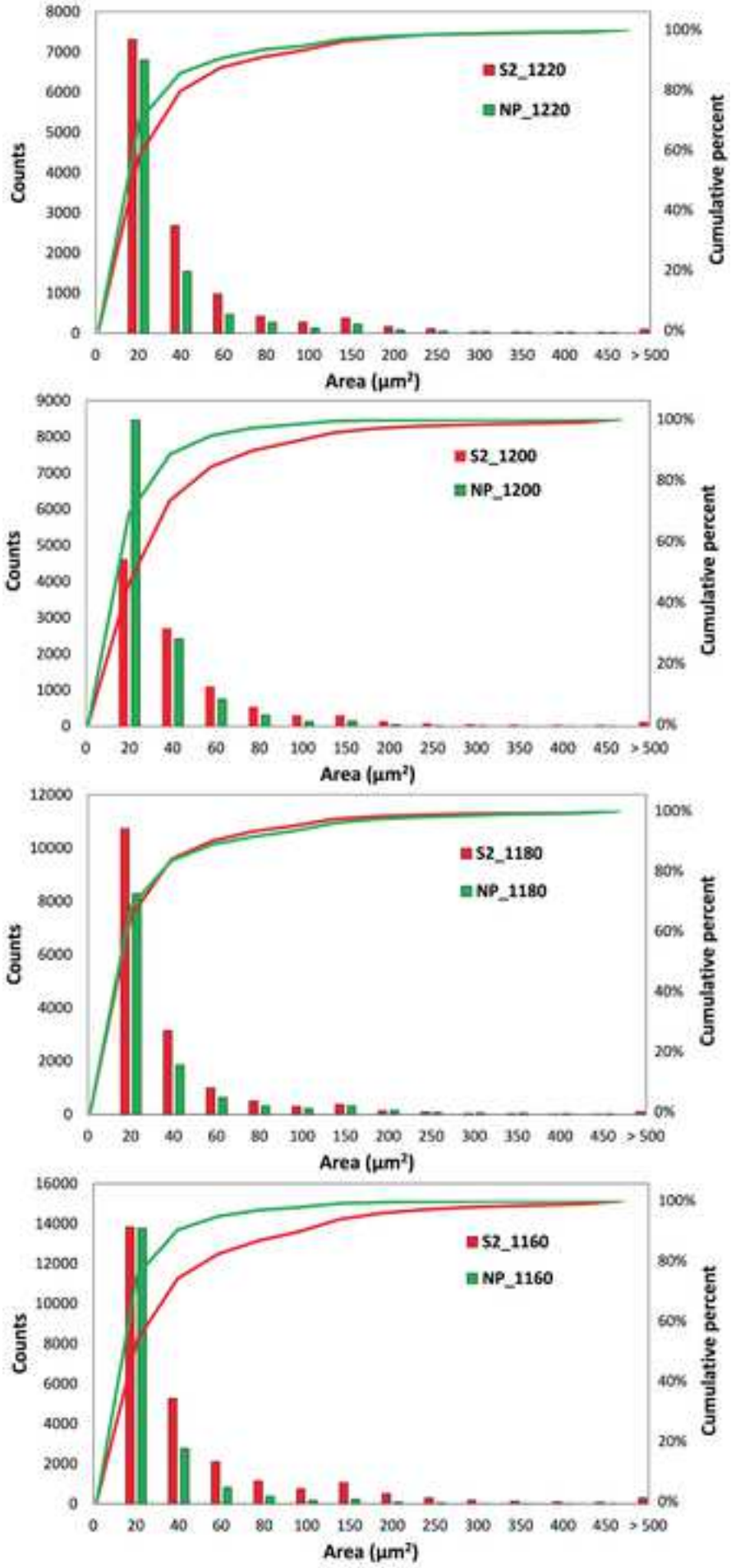

Figure 10



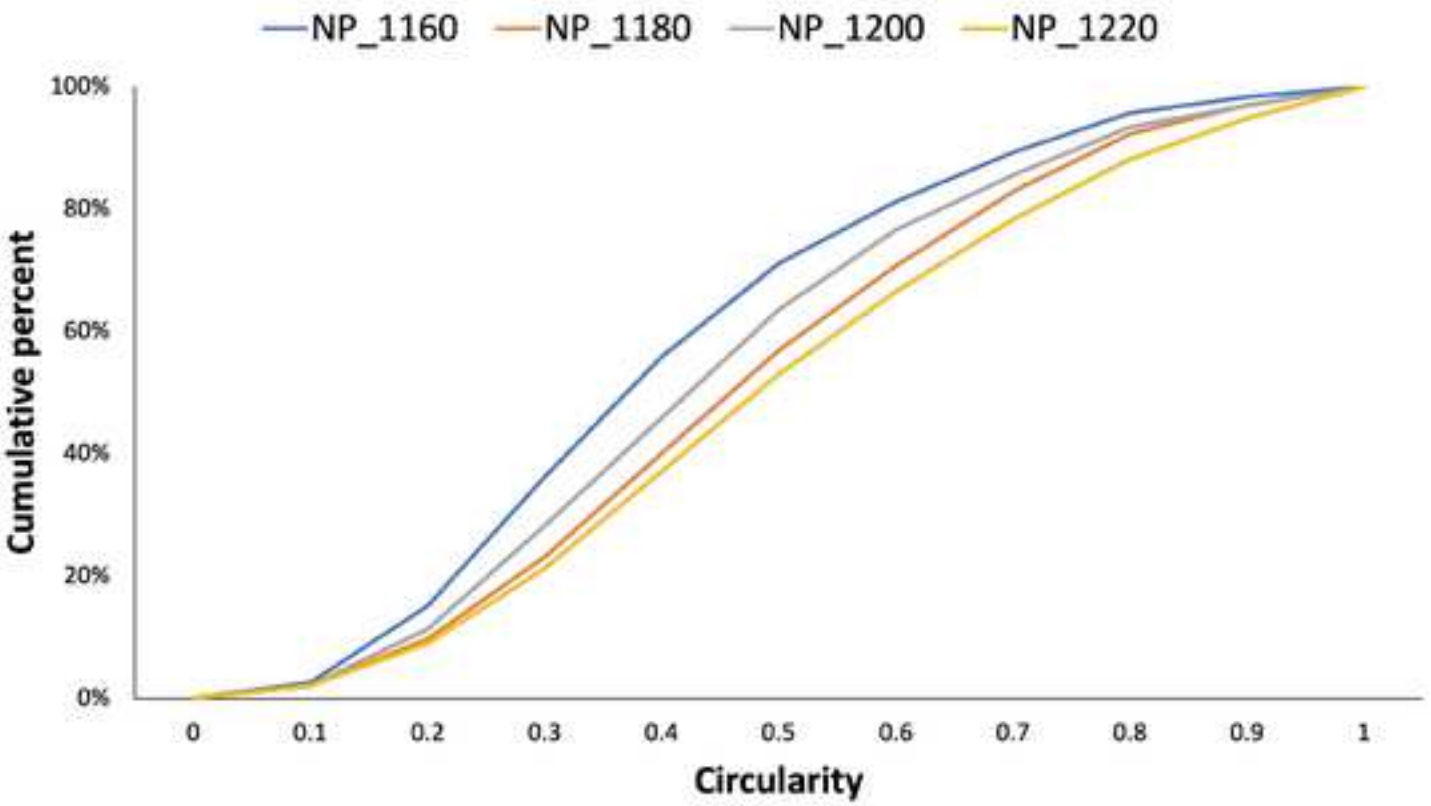


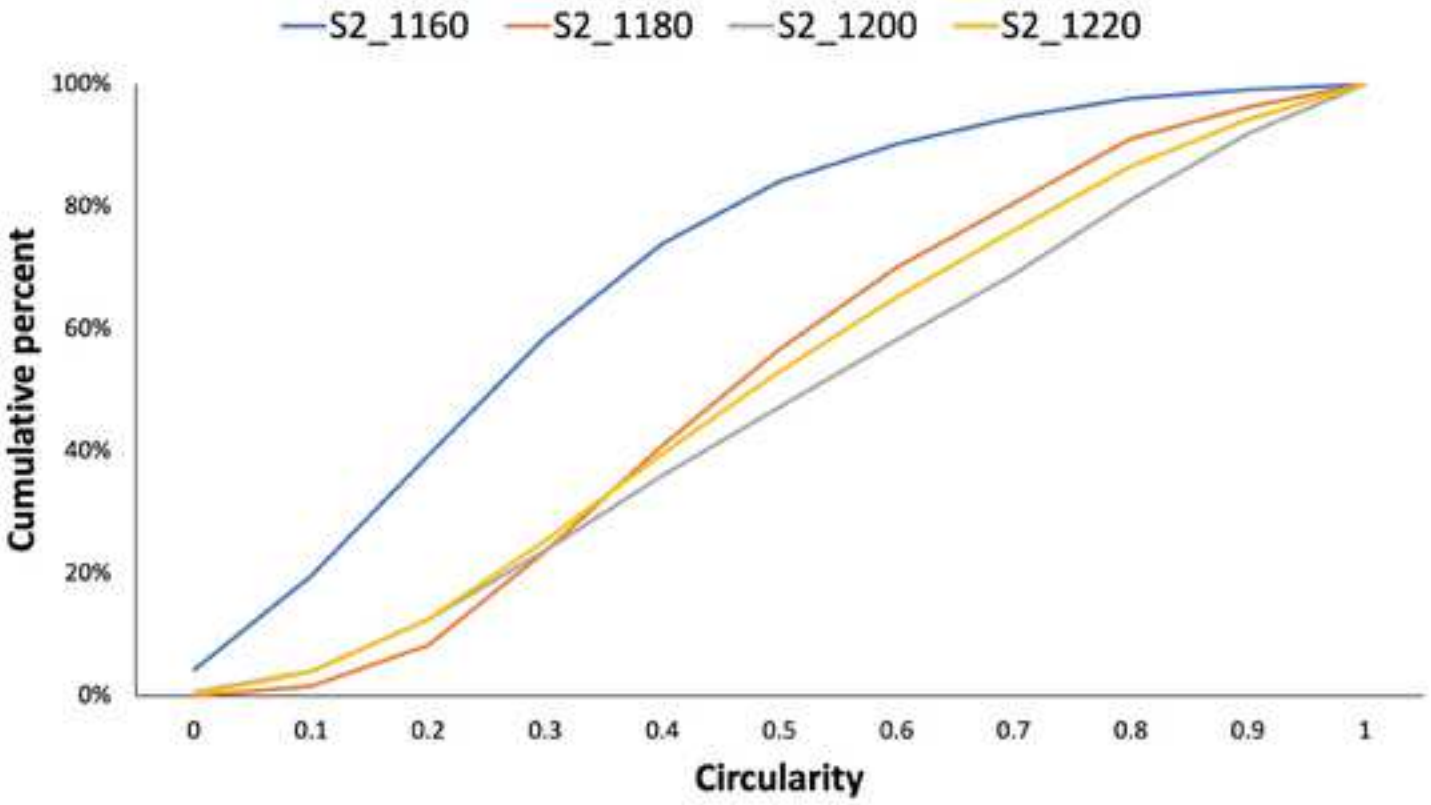

**Table 1S. Number of pores > 5µm² and their distribution in the chosen bin limits.**

| bin limits | 1220 | 1220NP | 1200 | 1200NP | 1180 | 1180NP | 1160 | 1160NP |
|---|---|---|---|---|---|---|---|---|
| 20 | 7313 | 6805 | 3755 | 8463 | 10728 | 8294 | 13838 | 13766 |
| 40 | 2678 | 1546 | 1357 | 2410 | 3148 | 1864 | 5267 | 2765 |
| 60 | 981 | 474 | 578 | 747 | 1002 | 640 | 2107 | 816 |
| 80 | 431 | 274 | 337 | 309 | 509 | 319 | 1153 | 377 |
| 100 | 280 | 128 | 188 | 133 | 303 | 225 | 760 | 175 |
| 150 | 379 | 226 | 340 | 142 | 378 | 319 | 1055 | 230 |
| 200 | 163 | 84 | 178 | 35 | 141 | 154 | 516 | 82 |
| 250 | 112 | 50 | 120 | 14 | 94 | 75 | 305 | 34 |
| 300 | 35 | 40 | 51 | 9 | 44 | 61 | 188 | 15 |
| 350 | 35 | 24 | 41 | 7 | 34 | 51 | 130 | 8 |
| 400 | 24 | 21 | 48 | 5 | 17 | 31 | 98 | 9 |
| 450 | 22 | 17 | 29 | 5 | 16 | 24 | 71 | 8 |
| > 500 | 100 | 66 | 198 | 7 | 102 | 99 | 297 | 19 |
| **SUM** | 12553 | 9755 | 7220 | 12286 | 16516 | 12156 | 25785 | 18304 |

**Table 2S. Percentage of pores > 5µm² and their distribution in the chosen bin limits.**

| bin limits | 1220 | 1220NP | 1200 | 1200NP | 1180 | 1180NP | 1160 | 1160NP |
|---|---|---|---|---|---|---|---|---|
| 20 | 58.26% | 69.76% | 52.01% | 68.88% | 64.96% | 68.23% | 53.67% | 75.21% |
| 40 | 21.33% | 15.85% | 18.80% | 19.62% | 19.06% | 15.33% | 20.43% | 15.11% |
| 60 | 7.81% | 4.86% | 8.01% | 6.08% | 6.07% | 5.26% | 8.17% | 4.46% |
| 80 | 3.43% | 2.81% | 4.67% | 2.52% | 3.08% | 2.62% | 4.47% | 2.06% |
| 100 | 2.23% | 1.31% | 2.60% | 1.08% | 1.83% | 1.85% | 2.95% | 0.96% |
| 150 | 3.02% | 2.32% | 4.71% | 1.16% | 2.29% | 2.62% | 4.09% | 1.26% |
| 200 | 1.30% | 0.86% | 2.47% | 0.28% | 0.85% | 1.27% | 2.00% | 0.45% |
| 250 | 0.89% | 0.51% | 1.66% | 0.11% | 0.57% | 0.62% | 1.18% | 0.19% |
| 300 | 0.28% | 0.41% | 0.71% | 0.07% | 0.27% | 0.50% | 0.73% | 0.08% |
| 350 | 0.28% | 0.25% | 0.57% | 0.06% | 0.21% | 0.42% | 0.50% | 0.04% |
| 400 | 0.19% | 0.22% | 0.66% | 0.04% | 0.10% | 0.26% | 0.38% | 0.05% |
| 450 | 0.18% | 0.17% | 0.40% | 0.04% | 0.10% | 0.20% | 0.28% | 0.04% |
| **SUM** | 100% | 100% | 100% | 100% | 100% | 100% | 100% | 100% |
| >100 | 9.16% | 6.72% | 16.52% | 2.91% | 6.84% | 8.55% | 13.26% | 3.17% |
| <60 | 79.59% | 85.61% | 70.80% | 88.50% | 84.02% | 83.56% | 74.09% | 90.31% |

**Table 3S. Cumulative percentage of pores > 5µm² in the chosen bin limits.**

| bin limits | 1220 | 1220NP | 1200 | 1200NP | 1180 | 1180NP | 1160 | 1160NP |
|---|---|---|---|---|---|---|---|---|
| 20 | 58% | 70% | 52% | 69% | 65% | 68% | 54% | 75% |
| 40 | 80% | 86% | 71% | 88% | 84% | 84% | 74% | 90% |
| 60 | 87% | 90% | 79% | 95% | 90% | 89% | 82% | 95% |
| 80 | 91% | 93% | 83% | 97% | 93% | 91% | 87% | 97% |
| 100 | 93% | 95% | 86% | 98% | 95% | 93% | 90% | 98% |
| 150 | 96% | 97% | 91% | 99% | 97% | 96% | 94% | 99% |
| 200 | 97% | 98% | 93% | 100% | 98% | 97% | 96% | 99% |
| 250 | 98% | 98% | 95% | 100% | 99% | 98% | 97% | 100% |
| 300 | 99% | 99% | 96% | 100% | 99% | 98% | 98% | 100% |
| 350 | 99% | 99% | 96% | 100% | 99% | 99% | 98% | 100% |
| 400 | 99% | 99% | 97% | 100% | 99% | 99% | 99% | 100% |
| 450 | 99% | 99% | 97% | 100% | 99% | 99% | 99% | 100% |
| > 500 | 100% | 100% | 100% | 100% | 100% | 100% | 100% | 100% |
| **SUM** | 100% | 100% | 100% | 100% | 100% | 100% | 100% | 100% |